Article

N-Based Polydentate Ligands and Corresponding Zn(II) Complexes: A Structural and Spectroscopic Study

Giorgio Volpi *, Stefano Zago, Roberto Rabezzana, Eliano Diana, Emanuele Priola, Claudio Garino and Roberto Gobetto

Department of Chemistry, University of Turin, Via P. Giuria, 7, 10125 Turin, Italy
* Correspondence: giorgio.volpi@unito.it

Abstract: Herein, the structural and photophysical features of two N-based polydentate ligands and the corresponding Zn(II) complexes are investigated. The obtained compounds were characterized using different spectroscopic techniques and their optical properties are discussed in relation to their chemical structure, defined by single-crystal X-ray diffraction and mass spectrometry. The spontaneous and quantitative complexation, investigated by UV-Vis, fluorescence, NMR, IR spectroscopies and mass spectrometry, makes these N-based polydentate ligands interesting candidates for possible applications in chelation therapy and in Zn(II) sensors.

Keywords: polydentate ligand; chelation therapy; Zn(II) sensor

1. Introduction

The human body contains up to several grams of Zn(II), making this element the second most abundant transition metal cation. Biological functions of Zn(II) have been reported for different purposes: it is required for the turnover of more than 300 catalytically active Zn(II) metal-proteins, as well as more than 2000 Zn(II)-dependent transcription factors [1]. Zn(II) is found at high concentrations, especially in the brain, pancreas and spermatozoa, and can be visualized with fluorescent dyes [2,3]. However, the biological functions of free or complexed Zn(II) are less certain. Recently, the exceptionally high intracellular Zn(II) concentration of β-cells (cells that produce insulin) has been widely investigated; indeed, β-cell insulin granules contain up to 20 mM Zn(II) compared to 2–10 μM in the Zn(II)-rich compartments of most other cell types. In addition, labile Zn(II) in the brain is reported to have a key role in the vesicles of presynaptic neurons, modulating the functions of fundamental ion channels and receptors [4–6].

A specific range of concentrations of metal ions in the body is required to ensure normal metabolic activities and physiological functions, as well as a healthy life. Contrariwise, the accumulation of metal ions (i.e., iron, lead, copper and zinc) in any organ, tissue, cellular or sub-cellular compartment represents a dangerous prognostic factor for many disorders and illness. The use of chelating drugs can re-equilibrate the metal imbalance and treat the associated diseases. For example, deferoxamine, deferiprone, deferasirox and their combinations are commonly used drugs for the medical treatment of Fe(III) overload in thalassaemia [7] and the chelating drugs penicillamine and triethylenetetramine are often used for Cu(II) overload in Wilson's disease [8–10]. Similarly, many other organic ligands are employed for the detoxification of different transition metal ions [11].

In this regard, polydentate ligands fill a unique area, due to their chemical and structural behaviours. They have been extensively studied because they integrate the properties of large-sized molecules, such as structural tunability and high selectivity, moderate manufacturing costs, positive pharmaco-kinetic behaviour and availability. Well-documented cases, such as triethylenetetramine, ethylenediaminetetraacetate (EDTA), cyclodextrins, substituted porphyrins and crown ethers, represent useful scaffolds between aromatic

ligands and functional structures [12,13]. Over the past few decades, polydentate ligand chemistry has been widely investigated and innovative synthetic approaches have been reported to collect new molecular skeletons with different binding properties, geometries, sizes and solubility [14–19]. New polydentate ligands with specific properties persist as a sought-after item for many innovative technological applications [20,21]. In general, polydentate ligands and their corresponding complexes can be utilized in various biomedical and pharmaceutical contexts, such as in drug delivery, biomaterials and diagnostic agents, ensuring minimal toxicity and compatibility with biological systems.

Initially, polydentate ligand derivatives captured escalating focus for their intriguing skeleton, and then for their use in supramolecular architectures [22–24], catalysis [25,26], high selectivity for ions and small-molecules recognition, supramolecular chemistry [27,28] and as chelating drugs for medical treatment [29–35]. In 2002, Zhao and Moore highlighted the structural relevance of the imine bond as a compositional unit in previously reported N-polydentate ligands such as macrocycles [36]. In particular, imine-containing phenylene portions are a significant subclass of shape-persistent products, because of their hetero-polydentate ligand capacity [37,38]. Phenylene-imine bonds have a few possible conformations, and the structural rigidity turns them into perfect systems and building blocks for larger structures, starting from macrocycles to open-chain polydentate ligands. Furthermore, the incorporation of substituent groups and N-heteroatoms into the backbone allows for powerful transition metal ion chelation along with the tuning of the optical and physical behaviour of the entire system [39].

Herein, we report the use of two N-based polydentate ligands (see Figure 1) obtained from common diamine and di-ketone precursors in a condensation process involving two consecutive imine-bond formations and a successive reduction. Recently, D. Carbajo et al. employed similar di-aldehyde (instead of ketone), obtaining innovative N-based polydentate ligands and macrocycles, as reported by the authors: "*these systems open the door to their use in stimuli-responsive materials with appealing properties*" [40]. These two ligands (**L1** and **L2**) represent the N-based polydentate nucleus for the spontaneous formation of the corresponding new Zn(II) complexes ([Zn**L1**]$^{2+}$ and [Zn**L2**]$^{2+}$). The complexation reaction has been investigated for possible therapeutic applications as chelating drugs or sensitive fluorescence 'turn-on' chemo-dosimeters [41–45].
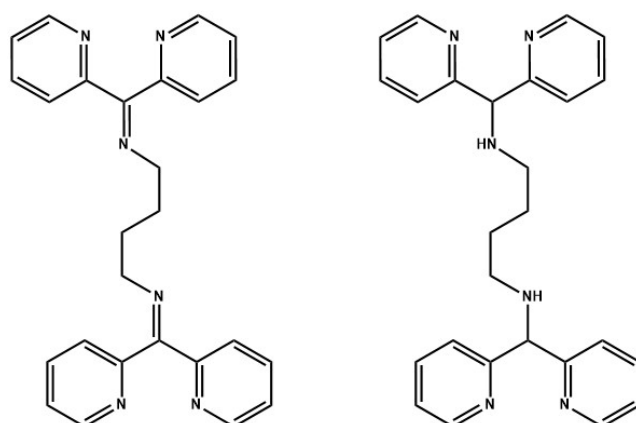

Figure 1. Chemical structures of the N-based polydentate ligands **L1** and **L2**.

2. Results and Discussion

2.1. Complexation Behaviour

The employed ligands contain six N-atoms which can potentially act as coordinating sites for metal–ligand chelation. Each ligand has four pyridinic nitrogen atoms plus two N-atoms from imine (**L1**) or amine (**L2**) groups, making these compounds interesting candidates for removing heavy metals from solutions, as well as for possible therapeutic applications as chelating drugs. To investigate the coordinating abilities of **L1** and **L2**, we prepared methanolic solutions of the ligands and added increasing equivalents of

Zn(NO$_3$)$_2$, while monitoring the evolution of the ^{1}H NMR signals (see Figure 2) and the UV-Vis absorption features (see Figure 3).
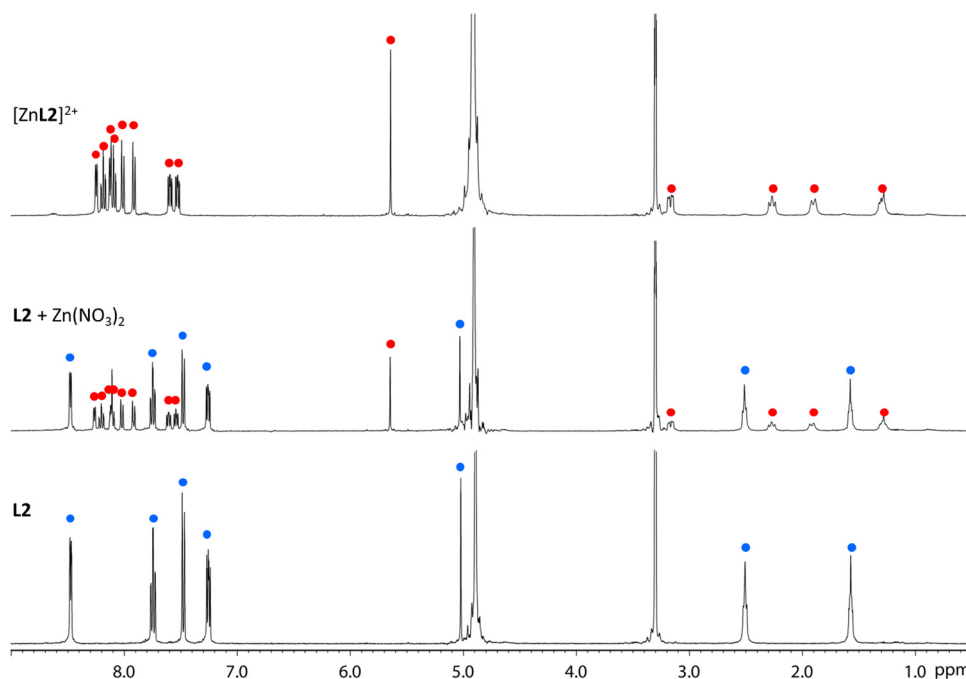

Figure 2. ^{1}H NMR of a deuterated methanolic solution of **L2** (blue dots) with increasing quantities (0.5 eq) of Zn(NO$_3$)$_2$, forming [Zn**L2**]$^{2+}$ (red dots).
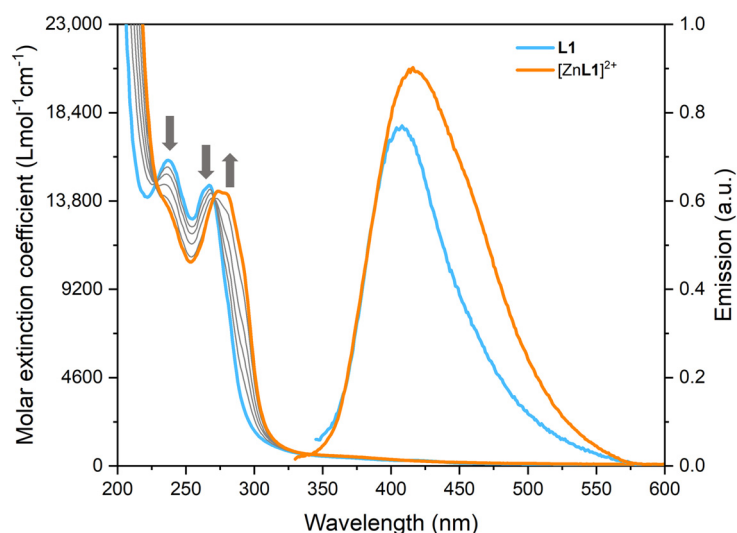

Figure 3. UV-Vis absorption and emission spectra of **L1** and the corresponding Zn(II) complex [Zn**L1**]$^{2+}$ (methanol, 25 °C, 10^{-5} M). Grey lines represent absorption after different additions of Zn(NO$_3$)$_2$ (0.2 eq each) to the **L1** solution.

Compounds **L1** and **L2** show a similar structure, with the important difference of the imino/amino bonds (see Figure S1 for the ^{1}H NMR spectrum for **L1** and Figure 2 for **L2**) [46]. In the ^{1}H NMR spectrum, **L1** exhibits eight multiplets corresponding to the sixteen pyridine protons (range 6–9 ppm) and two multiplets corresponding to the eight methylene protons of the alkyl chain (range 1–4 ppm). Similarly, **L2** exhibits four multiplets corresponding to the sixteen pyridine protons (range 6–9 ppm), with one singlet associated with the two methine proton (at about 5 ppm) confirming the reduction of the imino group, and two multiplets corresponding to the eight methylene protons of the alkyl chain (in the

range 1–4 ppm). In the case of **L2,** the high symmetry of the skeleton greatly simplifies the spectrum with respect to the complexity of **L1,** in which the imine bonds imply the asymmetry of the pyridine rings. These considerations are further confirmed by the ^{13}C NMR spectra where, in particular, the imine (quaternary carbon signal at 166.5 ppm for **L1**) and the amine (68.4 ppm signal for **L2**) signals are clearly recognisable.

In the ^{1}H and ^{13}C NMR spectra of the corresponding Zn(II) complexes, [Zn**L1**]$^{2+}$ and [Zn**L2**]$^{2+}$, all the signals are shifted compared to those of the employed ligands, providing clear evidence of the complexation that occurred with the Zn(II) ion. [Zn**L1**]$^{2+}$ and [Zn**L2**]$^{2+}$ show a very similar resonance pattern that highlights the asymmetrical nature of the coordinated pyridine rings on the Zn(II) centre (see Figure S1 for the ^{1}H NMR spectrum of [Zn**L1**]$^{2+}$ and Figure 2 for [Zn**L2**]$^{2+}$). The complexation reaction is spontaneous and immediate, as shown in Figures 2 and 3. Indeed, the addition of sub-stoichiometric amounts of Zn(NO$_3$)$_2$ to a methanolic solution of **L2** results in the progressive formation of [Zn**L2**]$^{2+}$ and the concomitant disappearance of the free **L2**. The octahedral coordination of **L2** on the metal centre (confirmed by single crystal XRD data, see Section 2.4) implies symmetry breaking, with the splitting of the ^{1}H NMR signals of the coordinate pyridine rings and the aliphatic chain (four signals for the diastereotopic methylene protons, see Figure 2). Conversely, in the case of [Zn**L1**]$^{2+}$, the protons of the aliphatic chain remain isochronous (2 methylene signals, see Figure S1), proving a tetrahedral coordination. This inference is further supported by the DFT optimised geometries of [Zn**L1**]$^{2+}$ and [Zn**L2**]$^{2+}$ computed in methanol solution (see Figure S2).

Additionally, the complexation monitored by UV-Vis absorption spectroscopy (10^{-5} M methanol solutions at 25 °C) confirms the complete conversion of each ligand into a corresponding single product (presence of isosbestic points, see Figure 3 for **L1** and [Zn**L1**]$^{2+}$ and Figure S3 for **L2** and [Zn**L2**]$^{2+}$).

2.2. Spectroscopic Characterization

The absorption and emission spectra of **L1**, **L2**, [Zn**L1**]$^{2+}$ and [Zn**L2**]$^{2+}$ in methanol solutions are reported in Figure 3 and in Figure S3, whereas selected optical data are collected in Table 1.

Table 1. Optical characterization of **L1**, **L2** and the corresponding Zn(II) complexes [Zn**L1**]$^{2+}$ and [Zn**L2**]$^{2+}$ (methanol at 25 °C, concentrations 10^{-5} M).

Compound	λ_{abs} (nm)	log ε (L mol^{-1} cm^{-1})	λ_{em} (nm)	Stokes Shift (cm^{-1})
L1	238 267	4.17 4.20	407	12,883
[ZnL1]$^{2+}$	278	4.15	418	12,048
L2	257 (sh) 262 272 (sh)	4.10 4.12 4.03	406	13,538
[ZnL2]$^{2+}$	257 266 272	4.10 4.10 4.08	406	12,134

L1 shows two principal bands, at 238 nm and 267 nm, with almost no absorption beyond 330 nm. The absorption profile of **L2**, which represents the corresponding reduced form of **L1** (from imine to amine), conversely shows a single band centred at 262 nm with two defined shoulders at 257 and 272 nm.

The complex [Zn**L1**]$^{2+}$ shows a noticeable change in the absorption profile, compared to the corresponding free ligand: the first band at 238 nm (well defined for **L1**) decreases in [Zn**L1**]$^{2+}$, while the second band is red shifted at 278 nm. The compound [Zn**L2**]$^{2+}$ displays a more structured band centred at 266 nm (surrounded by two shoulders more evident than for the free ligand), corresponding to n→π* and π→π* transitions.

All the studied compounds showed an appreciable emission between 350 and 550 nm, with emission maxima at about 410 nm (excitation wavelength at 300 nm). The modifications

of the ligand emission after the addition of $Zn(NO_3)_2$ are reported in Figures 3 and S13). The emission intensity increased after complexation with Zn(II), showing a little red-shift (11 nm) in the case of $[ZnL1]^{2+}$ in comparison to the free **L1** (see Table 1).

Solid state ATR-FTIR spectra of **L1** and **L2** and the corresponding $[ZnL1]^{2+}$ and $[ZnL2]^{2+}$ complexes are reported in the Supplementary Materials (see Figures S4 and S5). A DFT modelling of **L1**, **L2**, $[ZnL1]^{2+}$ and $[ZnL2]^{2+}$ was performed to check the vibrational assignments. In order to evaluate the effect of the Zn(II) coordination on the vibrational modes of the ligands, we focused on a few vibrational modes, in particular the symmetric ν_{CC} and ν_{CN} of the pyridyl ring and the $\nu_{C=N}$ and ν_{C-N} of imine and the corresponding amine of **L2**. The coordination of pyridine to Zn(II) induces a little shortening of the C-C bonds with a shift of ν_{CC} and ν_{CN} and br_{ring} to higher wavenumbers, respectively, 1580, 1482 and 992 cm^{-1} in py [47] and 1609, 1491 and 1016 cm^{-1} in $[ZnCl_2(py)_2]$ [48]. In **L1**, the doublet at 1572 and 1565 cm^{-1}, attributable to ν_{CC}, shifted to 1583 and 1572 cm^{-1} in $[ZnL1]^{2+}$, and the doublet at 1001 and 994 cm^{-1}, attributable to br_{ring}, shifted to 1019 and 1018 cm^{-1}. The imide $\nu_{C=N}$ stretching, attributable to 1634 cm^{-1} in **L1**, remained almost unchanged in $[ZnL1]^{2+}$, with a modest shift to 1683 cm^{-1} in $[ZnL1]^{2+}$, supporting the involvement of only pyridyl nitrogen in Zn coordination and the tetrahedral coordination of **L1** in $[ZnL1]^{2+}$.

In **L2**, the ν_{NH} at 3289 and 3261 cm^{-1}, because of the Zn(II) coordination, underwent a shift to lower wavenumbers and a broadening of the bands due to the hydrogen bond with NO_3^- groups. Similar to **L1**, the symmetric ν_{CC} may be assigned to 1586 and 1568 cm^{-1} in **L2**, shifted to 1601 and 1586 cm^{-1} in $[ZnL2]^{2+}$; br_{ring}, assignable in **L2** to the mode at 994 cm^{-1}, shifted to 1018 cm^{-1} in $[ZnL2]^{2+}$. The infrared spectra of both $[ZnL1]^{2+}$ and $[ZnL2]^{2+}$ showed the characteristic bands of the nitrate anion, with a medium-strong band at 1376 cm^{-1} due to asymmetric N-O stretching modes and a medium band at 828 cm^{-1} assignable to symmetric ν_{NO}. These nitrate modes do not show variation with respect to ionic nitrate groups of common salts, such as $ZnNO_3$ or $NaNO_3$.

2.3. Mass Spectrometry Characterization

The ESI-MS spectra of **L1**, **L2** and their corresponding Zn(II) complexes are reported in the Supplementary Materials (see Figures S6–S13). Collected spectra show the molecular peaks of the protonated form $[L+H]^+$ for **L1** and **L2** (see Figures S6 and S8, respectively) in methanol solutions (with 2% of formic acid). MS/MS experiments (see Figures S7 and S9) highlight similar fragmentation patterns for **L1** and **L2** species. Protonation due to formic acid likely occurs on the imine and amine N atoms, respectively, and subsequent heterolytic C-N cleavage yields the neutral fragments coming from the di-pyridine-ketone precursor, i.e., $C_{11}H_9N_3$ for **L1** and $C_{11}H_{11}N_3$ for **L2**.

The mass spectra of the corresponding complex solutions exhibited abundant peaks ascribed to $[ZnL1]^{2+} = C_{26}H_{24}N_6Zn$ (calculated average mass $m/z = 242$; found $m/z = 242$) and to $[ZnL2]^{2+} = C_{26}H_{28}N_6Zn$ (calculated average mass $m/z = 244$; found $m/z = 244$) (see Figures S10 and S12). The other signals in the spectra may be assigned either to ligand fragmentation or to clustering reactions taking place in the gas phase. Furthermore, the experimental isotopic distributions for all the observed ions fit nicely with the calculated isotopic simulation, thus representing additional proofs for product assignment; as can be observed, Figures S11 and S13 report as examples the cases of $[ZnL1]^{2+}$ and of $[ZnL2]^{2+}$, respectively.

2.4. Structural Characterization

The ligand **L1** crystallized from ethanol by slow evaporation in yellow prisms. The space group type is monoclinic $P2_1/c$, with half a molecule in the asymmetric unit and the entire molecule generated by an inversion centre. The imide nature is clear by the distance between C3 and N1 (1.276(5) Å, typical of imides, with respect to 1.493(6) Å found for **L2** in the complex $[ZnL2]^{2+}$) and for the planarity of the nearby fragments. The two pyridine groups are staggered to each other, to minimize the steric hindrance (see Figure 4).

Moreover, in the crystal packing, the molecules are disposed orthogonally, interacting with dispersion interactions and C-H⋯π contacts (d(C-H⋯π)= 3.662 Å, see Figure 4, right).
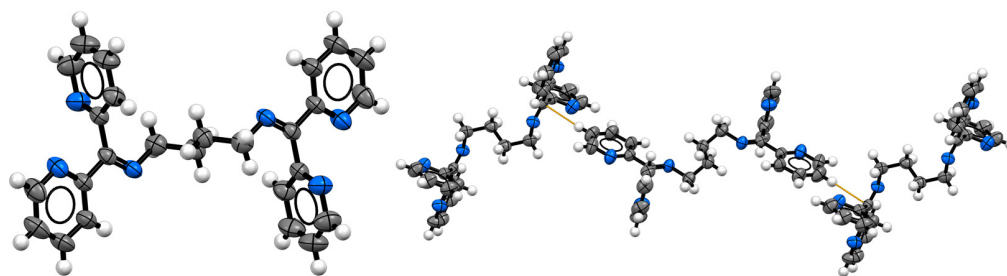

Figure 4. ORTEP plot of the molecule **L1** (**left**) and the corresponding weak contacts in the crystal packing (**right**) (50% probability) (colour code: grey, carbon; blue, nitrogen; white, hydrogen).

On the other hand, crystals of [Zn**L2**](NO$_3$)$_2$·DMF have been obtained from DMF. The complex crystallizes as DMF solvate in the monoclinic non-centrosymmetric *Cc* space group type. Neither the nitrate counterion nor the DMF are bonded directly to the metal centre, while the Zn(II) is completely surrounded by the six coordination sites of **L2** to form a nearly regular octahedron (see Figure 5, left, and Table 2).
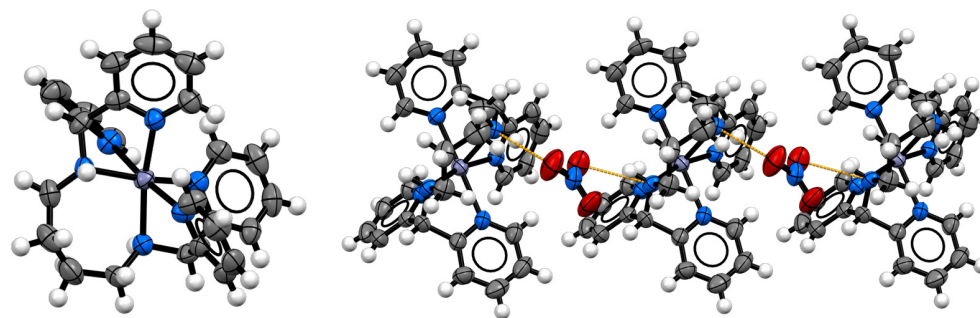

Figure 5. ORTEP plot of the molecule [Zn**L2**](NO$_3$)$_2$·DMF (**left**) and the corresponding weak contacts in the crystal packing (**right**) (50% probability) (colour code: violet, zinc; grey, carbon; blue, nitrogen; red, oxygen; white, hydrogen).

Table 2. Distances of bonds of ligand sites around the Zn(II) ion.

d(Zn-N)	Distance (Å)
Zn-N1	2.231(4)
Zn-N2	2.105(4)
Zn-N3	2.160(5)
Zn-N4	2.126(4)
Zn-N5	2.143(4)
Zn-N6	2.240(4)

The Zn-N distances are irregular, as are the angles, specifically the ones regarding the bonds with the most distant pyridyl group, probably due to the steric hindrance internal of L2 (see Tables 2 and S3). In the crystal packing, it is worth noting the presence of hydrogen-bond-forming chains between one of the nitrate and the complexes through the amine hydrogens (d(N4-H⋯O2) = 2.983(8) Å, see Figure 5, right).

3. Materials and Methods

3.1. Experimental Details

All solvents and raw materials were used as received from commercial suppliers (Sigma-Aldrich and Alfa Aesar, Milano, Italy) without further purification. TLC was performed on Fluka silica gel TLC-PET foils GF 254, particle size 25 nm, medium pore

diameter 60 Å. Column chromatography was performed on Sigma-Aldrich silica gel 60 (70–230 mesh ASTM).

^{1}H and ^{13}C NMR spectra were recorded on a JEOL ECP 400 FT-NMR spectrometer (^{1}H NMR operating frequency 400 MHz). Chemical shifts are reported relative to TMS (δ = 0) and referenced against solvent residual peaks. The following abbreviations are used: s (singlet), d (doublet), t (triplet), dd (doublet of doublets), m (multiplet). Mass spectra were recorded on a Thermo-Finnigan Advantage Max Ion Trap Spectrometer equipped with an electrospray ion source (ESI) in positive and negative ion acquiring mode and with a Sciex Triple Quad 5500 equipped with a Turbo V™ source in positive electrospray mode. UV-Vis absorption spectra were recorded on a Cary60 spectrometer; infrared spectra were recorded on solid samples with a PerkinElmer Spectrum Two FT-IR Spectrometer equipped with a Universal Attenuated Total Reflectance accessory. DFT calculations were performed with the Gaussian 16 program package [49], employing the density functional theory (DFT) method with the Becke three-parameter hybrid functional [50] and the Lee–Yang–Parr gradient-corrected correlation functional (B3LYP) [51]. The solvent effect was included by using the conductor-like polarizable continuum model (CPCM) with methanol as the solvent [52,53]. The 6–31g(d,p) basis set was used for all atoms [54]. Geometries were optimized without any symmetry constraints and harmonic frequencies were computed. The nature of the optimized structures was verified by using harmonic vibrational frequency calculations. No imaginary frequencies were found, thus indicating we had located the minima on the potential energy surfaces. Molecular-graphic images were produced by using the UCSF Chimerax package from the Resource for Biocomputing, Visualization, and Informatics at the University of California, San Francisco (supported by NIH P41 RR001081) [55].

Single crystal data were collected on a Gemini R Ultra diffractometer (Agilent Technologies UK Ltd., Oxford, UK) using graphite-monochromatic Mo Kα radiation (λ = 0.7563 Å) with the ω-scan method. Copper-derived radiation was preferred for the cases of very weakly diffracting crystals. CrysAlisPro v42 software was used for retrieving cell parameters, for performing data reduction and for absorption correction (with multi-scan technique). All structures were solved with direct methods using ShelXS-14 and refined with full-matrix least-squares on F2 using the SHELXL-14 using the Olex2 program. All non-hydrogen atoms were anisotropically refined. Hydrogen atoms were calculated and were riding on the corresponding atom. Structure images were obtained using Mercury 2023.1.0 software. Crystal data and refinement, selected bond lengths and angle amplitudes and asymmetric units of compounds are reported in ESI. The crystallographic data for the crystallized compounds are deposited within the Cambridge Crystallographic Data Centre as supplementary publications under the CCDC numbers 2289875-2289876. This information can be obtained free of charge from the Cambridge Crystallographic Data Centre.

3.2. Synthesis

The synthetic approach has been previously employed by us to successfully produce different ligands from the versatile di-pyridyl ketone reagent; the obtained derivatives show excellent coordination skills towards different metal ions [56,57]. The N-based polydentate ligands **L1** and **L2** were obtained as previously reported [56].

3.2.1. **L1**: N,N'-(Butane-1,4-diyl)bis(1,1-di(pyridin-2-yl)methanimine)

In 30 mL of methanol were mixed di-2-pyridyl ketone (839 mg, 4.56 mmol), butane-1,4-diamine (200 mg, 2.28 mmol, 0.5 eq) and 5 drops of acetic acid. After 4 h refluxing, the solution was cooled. The solvent evaporated under vacuum. The final product was obtained after column chromatography on silica gel, using CH_2Cl_2/CH_3OH (98:2) as eluent. Reaction yield: 906 mg, 2.16 mmol, 95%. ^{1}H NMR (methanol-d4, 400 MHz) δ: 8.59 (d, *J* = 5.0 Hz, 2H), 8.40 (d, *J* = 5.0 Hz, 2H), 8.07 (d, *J* = 8.0 Hz, 2H), 7.91 (t, *J* = 7.7 Hz, 2H), 7.87 (t, *J* = 7.7 Hz, 2H), 7.45 (dd, *J* = 7.7 Hz, *J* = 5.0 Hz, 2H), 7.39 (dd, *J* = 7.5 Hz, *J* = 4.9 Hz, 2H),

7.31 (d, *J* = 7.7 Hz, 2H), 3.37 (m, 4H), 1.74 (m, 4H) ppm. ^{13}C NMR (methanol-d4, 100 MHz) δ: 166.5, 156.2, 154.6, 148.9, 148.2, 137.1, 136.9, 124.6, 124.1, 123.7, 122.3, 53.1, 28.2 ppm. MS (ESI+) *m/z* calculated for [**L1**+H]$^+$ = C$_{26}$H$_{25}$N$_6$ *m/z* = 421.21; found *m/z* = 421.07.

3.2.2. **L2**: N^1,N^4-Bis(di(pyridin-2-yl)methyl)butane-1,4-diamine

The precursor **L1** (500 mg, 1.19 mmol) was reduced with an excess of NaBH$_4$ in methanol at 0 °C for 1 h. The solvent was removed under vacuum. Then, the obtained crude product was dissolved in CH$_2$Cl$_2$, and the solution extracted with water and brine and filtered and dried over Na$_2$SO$_4$. The solvent evaporated under vacuum. The oily product was obtained in quantitative yield: 504 mg, 1.19 mmol. ^{1}H NMR (methanol-d4, 400 MHz) δ: 8.46 (d, *J* = 5.0 Hz, 4H), 7.73 (t, *J* = 7.7 Hz, 4H), 7.46 (t, *J* = 7.9 Hz, 4H), 7.24 (dd, *J* = 7.5 Hz, *J* = 5.0 Hz, 4H), 5.01 (s, 2H), 2.49 (m, 4H), 1.56 (m, 4H) ppm. ^{13}C NMR (methanol-d4, 100 MHz) δ: 160.5, 148.6, 137.3, 122.6, 122.5, 68.4, 47.0, 27.0 ppm. MS (ESI+) *m/z* calculated for [**L2**+H]$^+$ = C$_{26}$H$_{29}$N$_6$ *m/z* = 425.24; found *m/z* = 425.10.

The Zn(II) complexes [Zn**L1**]$^{2+}$ and [Zn**L2**]$^{2+}$ were obtained in quantitative yield by the reaction of Zn(NO$_3$)$_2$ with a stoichiometric amount of the corresponding ligand in methanol at room temperature. All the complexes are uncoloured crystalline powders.

3.2.3. [Zn**L1**]$^{2+}$

^{1}H NMR (methanol-d4, 400 MHz) δ: 8.85 (m, 4H), 8.28 (t, *J* = 7.8 Hz, 2H), 8.16 (t, *J* = 7.8 Hz, 2H), 7.98 (dd, *J* = 7.5 Hz, *J* = 5.0 Hz, 2H), 7.78 (d, *J* = 7.8 Hz, 2H), 7.71 (dd, *J* = 7.8 Hz, *J* = 4.9 Hz, 2H), 7.50 (d, *J* = 7.9 Hz, 2H), 3.76 (m, 4H), 2.08 (m, 4H) ppm. ^{13}C NMR (methanol-d4, 100 MHz) δ: 168.0, 150.6, 149.7, 149.6, 148.0, 142.2, 138.2, 129.3, 128.2, 125.9, 124.5, 52.2, 27.0 ppm. MS (ESI+) *m/z* calculated for [Zn**L1**]$^{2+}$ = C$_{26}$H$_{24}$N$_6$Zn^{2+} *m/z* = 242.07; found *m/z* = 242).

3.2.4. [Zn**L2**]$^{2+}$

^{1}H NMR (methanol-d4, 400 MHz) δ: 8.25 (d, *J* = 5.0 Hz, 2H), 8.19 (t, *J* = 7.8 Hz, 2H), 8.12 (d, *J* = 5.0 Hz, 2H), 8.10 (t, *J* = 7.8 Hz, 2H), 8.01 (d, *J* = 7.8 Hz, 2H), 7.92 (d, *J* = 7.8 Hz, 2H), 7.60 (dd, *J* = 7.7 Hz, *J* = 5.1 Hz, 2H), 7.53 (dd, *J* = 7.7 Hz, *J* = 5.1 Hz, 2H), 5.64 (s, 2H), 3.16 (m, 2H), 2.27 (m, 2H), 1.90 (m, 2H), 1.23 (m, 2H) ppm. ^{13}C NMR (methanol-d4, 100 MHz) δ: 157.0, 155.4, 148.6, 147.9, 141.5, 141.0, 125.7, 125.5, 124.8, 124.1, 65.5, 49.1, 28.2 ppm. MS (ESI+) *m/z* calculated for [Zn**L2**]$^{2+}$ = C$_{26}$H$_{28}$N$_6$Zn^{2+} (calculated average mass: *m/z*= 244.08; found *m/z* = 244).

4. Conclusions

Two interesting N-based polydentate ligands have been synthesized and characterized in comparison with the corresponding Zn(II) complexes. The structure of the obtained compounds was determined using ^{1}H and ^{13}C NMR, UV-Vis absorption, emission and FT-IR spectroscopies, Electrospray Ionization Mass Spectrometry and X-Ray Diffraction. Obtained from a mild, straightforward and efficient preparation, the studied polydentate skeletons could inspire the design of a possible wide range of new ligands with different metal ion affinities.

The comparison between the structures of the free ligands **L1** and **L2** and corresponding Zn(II) complexes [Zn**L1**]$^{2+}$ and [Zn**L2**]$^{2+}$ shows an interesting modification in the spectroscopic properties. In particular, a noticeable change in the absorption profile (comparing the free ligand and the corresponding Zn(II) complex), a strong quenching in the emission along with appreciable shift and the splitting and shift of the NMR signals highlight the asymmetrical nature of the coordinated pyridine rings on the Zn(II) centre.

The proposed study shows that the investigated complexation reaction is spontaneous, instantaneous and complete, all key aspects for possible future applications.

Overall, these results encourage further studies on these N-based polydentate skeletons, aiming to introduce new functional groups, varying the chelating geometry and the electronic behaviours to further investigate the coordinating properties of these ligands.

In general, polypyridine compounds have shown promise in various medical applications due to their ability to form stable metal complexes. Furthermore, designing polypyridine-based materials for medical applications is a multidisciplinary endeavour that combines knowledge of chemistry, biology and materials science. In this context, it is essential to consider the specific requirements and challenges of each possible application to develop safe and effective solutions such as biocompatibility, stability, regulatory compliance and many others.

In conclusion, the synthetic accessibility and the demonstrated complete interactions with Zn(II) ions make these promising polydentate ligands interesting candidates for chelation therapy, Zn(II) sensors and possibly in metal ion removal, as recently reported for similar innovative structures [58–64].

Supplementary Materials: The following supporting information can be downloaded at: https://www.mdpi.com/article/10.3390/inorganics11110435/s1, Figure S1. ^{1}H NMR spectrum of **L1** and [Zn**L1**]$^{2+}$ in CD_3OD; Figure S2. DFT optimized structures of [Zn**L1**]$^{2+}$ and [Zn**L2**]$^{2+}$ in CD_3OD solution; Figure S3. UV-vis absorption and emission spectra of **L2** and the corresponding Zn(II) complex [Zn**L2**]$^{2+}$ (methanol, 25 °C, 10^{-5}M); Figure S4. Vibrational comparisons between **L1** and [Zn**L1**]$^{2+}$; Figure S5. Vibrational comparisons between ligand **L2** and macrocycle [Zn**L2**]$^{2+}$; Figure S6. ESI-MS mass spectrum of ligand **L1**; Figure S7. ESI-MS/MS mass spectrum of [**L1**+H]$^+$; Figure S8. ESI-MS mass spectrum of ligand **L2**; Figure S9. ESI-MS/MS mass spectrum of [**L2**+H]$^+$; Figure S10. ESI-MS mass spectrum of complex [Zn**L1**]$^{2+}$; Figure S11. Experimental and theoretical isotopic composition of the [Zn**L1**]$^{2+}$ ion; Figure S12. ESI-MS mass spectrum of complex [Zn**L2**]$^{2+}$; Figure S13. Experimental and theoretical isotopic composition of the [Zn**L2**]$^{2+}$ ion; Figure S14. ORTEP plot of asymmetric unit of **L1**; Figure S15. ORTEP plot of asymmetric unit of [Zn**L2**](NO$_3$)$_2$·DMF; Table S1. Crystal data and structure refinement for **L1**; Table S2. Bond Lengths for **L1**; Table S3. Bond Angles for **L1**; Table S4. Crystal data and structure refinement for [Zn**L2**](NO$_3$)$_2$·DMF; Table S5. Crystal data and structure refinement for [Zn**L2**](NO$_3$)$_2$·DMF; Table S6. Bond Angles for [Zn**L2**](NO$_3$)$_2$·DMF.

Author Contributions: Conceptualization, G.V. and C.G.; formal analysis, S.Z. and E.P.; investigation, G.V. and R.R.; resources, R.G. and E.D.; writing—original draft preparation, G.V. and R.R.; writing—review and editing, R.G. and C.G.; visualization, C.G.; supervision, G.V. All authors have read and agreed to the published version of the manuscript.

Data Availability Statement: The data presented in this study are available on request from the corresponding author.

Conflicts of Interest: The authors declare no conflict of interest.

References

1. Vahidi Ferdowsi, P.; Ng, R.; Adulcikas, J.; Sohal, S.S.; Myers, S. Zinc Modulates Several Transcription-Factor Regulated Pathways in Mouse Skeletal Muscle Cells. *Molecules* **2020**, *25*, 5098. [CrossRef] [PubMed]
2. Tang, J.; Yin, H.-Y.; Zhang, J.-L. Chapter One—Luminescent Zinc Complexes as Bioprobes for Imaging Molecular Events in Live Cells. In *Inorganic and Organometallic Transition Metal Complexes with Biological Molecules and Living Cells*; Lo, K.K.-W., Ed.; Academic Press: Cambridge, MA, USA, 2017; pp. 1–53; ISBN 978-0-12-803814-7.
3. Endo, I.; Nagamune, T. *Nano/Micro Biotechnology*; Springer Science & Business Media: Berlin/Heidelberg, Germany, 2010; ISBN 978-3-642-14946-7.
4. Horton, T.M.; Allegretti, P.A.; Lee, S.; Moeller, H.P.; Smith, M.; Annes, J.P. Zinc-Chelating Small Molecules Preferentially Accumulate and Function within Pancreatic β Cells. *Cell Chem. Biol.* **2019**, *26*, 213–222.e6. [CrossRef] [PubMed]
5. Das, R.K.; Pachapur, V.L.; Lonappan, L.; Naghdi, M.; Pulicharla, R.; Maiti, S.; Cledon, M.; Dalila, L.M.A.; Sarma, S.J.; Brar, S.K. Biological Synthesis of Metallic Nanoparticles: Plants, Animals and Microbial Aspects. *Nanotechnol. Environ. Eng.* **2017**, *2*, 18. [CrossRef]
6. Kikuchi, K.; Komatsu, K.; Nagano, T. Zinc Sensing for Cellular Application. *Curr. Opin. Chem. Biol.* **2004**, *8*, 182–191. [CrossRef]
7. Neufeld, E.J. Oral Chelators Deferasirox and Deferiprone for Transfusional Iron Overload in Thalassemia Major: New Data, New Questions. *Blood* **2006**, *107*, 3436–3441. [CrossRef]

8. Purchase, R. The Treatment of Wilson's Disease, a Rare Genetic Disorder of Copper Metabolism. *Sci. Prog.* **2013**, *96*, 19–32. [CrossRef]
9. Delangle, P.; Mintz, E. Chelation Therapy in Wilson's Disease: From d-Penicillamine to the Design of Selective Bioinspired Intracellular Cu(i) Chelators. *Dalton Trans.* **2012**, *41*, 6359–6370. [CrossRef]
10. Siegemund, R.; Lößner, J.; Günther, K.; Kühn, H.-J.; Bachmann, H. Mode of Action of Triethylenetetramine Dihydrochloride on Copper Metabolism in Wilson's Disease. *Acta Neurol. Scand.* **1991**, *83*, 364–366. [CrossRef]
11. Kontoghiorghes, G.J. Advances on Chelation and Chelator Metal Complexes in Medicine. *Int. J. Mol. Sci.* **2020**, *21*, 2499. [CrossRef]
12. Kim, K.; Murray, J.; Selvapalam, N.; Ko, Y.H.; Hwang, I. *Cucurbiturils: Chemistry, Supramolecular Chemistry and Applications*; WORLD SCIENTIFIC (EUROPE): London, UK, 2018; ISBN 978-1-84816-408-6.
13. Andreo, L.; Volpi, G.; Rossi, F.; Benzi, P.; Diana, E. Two-Step Synthesis of a New Twenty-Membered Macrocycle: Spectroscopic Characterization and Theoretical Calculations. *ChemistrySelect* **2022**, *7*, e202202564. [CrossRef]
14. Knipe, A.C. Crown Ethers. A New Aid to Synthesis and to Elucidation of Reaction Mechanisms. *J. Chem. Educ.* **1976**, *53*, 618. [CrossRef]
15. Evans, N.H. Chiral Catenanes and Rotaxanes: Fundamentals and Emerging Applications. *Chem. Eur. J.* **2018**, *24*, 3101–3112. [CrossRef] [PubMed]
16. Ji, X.; Ahmed, M.; Long, L.; Khashab, N.M.; Huang, F.; Sessler, J.L. Adhesive Supramolecular Polymeric Materials Constructed from Macrocycle-Based Host–Guest Interactions. *Chem. Soc. Rev.* **2019**, *48*, 2682–2697. [CrossRef] [PubMed]
17. Volpi, G.; Garino, C.; Priola, E.; Diana, E.; Gobetto, R.; Buscaino, R.; Viscardi, G.; Barolo, C. Facile Synthesis of Novel Blue Light and Large Stoke Shift Emitting Tetradentate Polyazines Based on Imidazo[1,5-a]Pyridine—Part 2. *Dye. Pigment.* **2017**, *143*, 284–290. [CrossRef]
18. Nelson, S.M. Developments in the Synthesis and Coordination Chemistry of Macrocyclic Schiff Base Ligands. *Pure Appl. Chem.* **1980**, *52*, 2461–2476. [CrossRef]
19. Wu, J.-R.; Yang, Y.-W. New Opportunities in Synthetic Macrocyclic Arenes. *Chem. Commun.* **2019**, *55*, 1533–1543. [CrossRef]
20. Ball, M.; Zhang, B.; Zhong, Y.; Fowler, B.; Xiao, S.; Ng, F.; Steigerwald, M.; Nuckolls, C. Conjugated Macrocycles in Organic Electronics. *Acc. Chem. Res.* **2019**, *52*, 1068–1078. [CrossRef]
21. Saha, S.K.; Dutta, A.; Ghosh, P.; Sukul, D.; Banerjee, P. Novel Schiff-Base Molecules as Efficient Corrosion Inhibitors for Mild Steel Surface in 1 M HCl Medium: Experimental and Theoretical Approach. *Phys. Chem. Chem. Phys.* **2016**, *18*, 17898–17911. [CrossRef]
22. Buston, J.E.H.; Young, J.R.; Anderson, H.L. Rotaxane-Encapsulated Cyanine Dyes: Enhanced Fluorescence Efficiency and Photostability. *Chem. Commun.* **2000**, 905–906. [CrossRef]
23. Fujiwara, T.; Muranaka, A.; Nishinaga, T.; Aoyagi, S.; Kobayashi, N.; Uchiyama, M.; Otani, H.; Iyoda, M. Preparation, Spectroscopic Characterization and Theoretical Study of a Three-Dimensional Conjugated 70 π-Electron Thiophene 6-Mer Radical Cation π-Dimer. *J. Am. Chem. Soc.* **2020**, *142*, 5933–5937. [CrossRef]
24. Mako, T.L.; Racicot, J.M.; Levine, M. Supramolecular Luminescent Sensors. *Chem. Rev.* **2019**, *119*, 322–477. [CrossRef] [PubMed]
25. Schettini, R.; Sicignano, M.; De Riccardis, F.; Izzo, I.; Della Sala, G. Macrocyclic Hosts in Asymmetric Phase-Transfer Catalyzed Reactions. *Synthesis* **2018**, *50*, 4777–4795. [CrossRef]
26. Aucagne, V.; Berná, J.; Crowley, J.D.; Goldup, S.M.; Hänni, K.D.; Leigh, D.A.; Lusby, P.J.; Ronaldson, V.E.; Slawin, A.M.Z.; Viterisi, A.; et al. Catalytic "Active-Metal" Template Synthesis of [2]Rotaxanes, [3]Rotaxanes, and Molecular Shuttles, and Some Observations on the Mechanism of the Cu(I)-Catalyzed Azide−Alkyne 1,3-Cycloaddition. *J. Am. Chem. Soc.* **2007**, *129*, 11950–11963. [CrossRef]
27. Peng, R.; Xu, Y.; Cao, Q. Recent Advances in Click-Derived Macrocycles for Ions Recognition. *Chin. Chem. Lett.* **2018**, *29*, 1465–1474. [CrossRef]
28. Mantooth, S.M.; Munoz-Robles, B.G.; Webber, M.J. Dynamic Hydrogels from Host-Guest Supramolecular Interactions. *Macromol. Biosci.* **2019**, *19*, 1800281. [CrossRef]
29. Zhou, T.; Ma, Y.; Kong, X.; Hider, R.C. Design of Iron Chelators with Therapeutic Application. *Dalton Trans.* **2012**, *41*, 6371–6389. [CrossRef]
30. Kim, J.-J.; Kim, Y.-S.; Kumar, V. Heavy Metal Toxicity: An Update of Chelating Therapeutic Strategies. *J. Trace Elem. Med. Biol.* **2019**, *54*, 226–231. [CrossRef]
31. Liu, Z.D.; Hider, R.C. Design of Clinically Useful Iron(III)-Selective Chelators. *Med. Res. Rev.* **2002**, *22*, 26–64. [CrossRef]
32. Roy, M.; Chakravarthi, B.V.S.K.; Jayabaskaran, C.; Karande, A.A.; Chakravarty, A.R. Impact of Metal Binding on the Antitumor Activity and Cellular Imaging of a Metal Chelator Cationic Imidazopyridine Derivative. *Dalton Trans.* **2011**, *40*, 4855–4864. [CrossRef]
33. Liu, Z.D.; Hider, R.C. Design of Iron Chelators with Therapeutic Application. *Coord. Chem. Rev.* **2002**, *232*, 151–171. [CrossRef]
34. Chaudhari, V.; Bagwe-Parab, S.; Buttar, H.S.; Gupta, S.; Vora, A.; Kaur, G. Challenges and Opportunities of Metal Chelation Therapy in Trace Metals Overload-Induced Alzheimer's Disease. *Neurotox. Res.* **2023**, *41*, 270–287. [CrossRef] [PubMed]
35. Bissani Gasparin, C.; Pilger, D.A. 8-Hydroxyquinoline, Derivatives and Metal-Complexes: A Review of Antileukemia Activities. *ChemistrySelect* **2023**, *8*, e202204219. [CrossRef]
36. Zhao, D.; Moore, J.S. Synthesis and Self-Association of an Imine-Containing m-Phenylene Ethynylene Macrocycle. *J. Org. Chem.* **2002**, *67*, 3548–3554. [CrossRef] [PubMed]

37. Akine, S.; Taniguchi, T.; Nabeshima, T. Synthesis and Crystal Structure of a Novel Triangular Macrocyclic Molecule, Tris(H$_2$saloph), H$_2$saloph=N,N′-Disalicylidene-o-Phenylenediamine. and Its Water Complex. *Tetrahedron Lett.* **2001**, *42*, 8861–8864. [CrossRef]

38. Curtis, N.F. Compounds of Amine-Imine Macrocycles: Syntheses and Structures of Compounds of Aza-Macrocycles with Amine-β-Imine Ring Segments. *Inorganica Chim. Acta* **2021**, *527*, 120164. [CrossRef]

39. Ma, J.; Vannam, R.; Terwilliger, D.W.; Peczuh, M.W. Synthesis, Structure and Reactivity of a Macrocyclic Imine: Aza-[13]-Macrodiolides. *Tetrahedron Lett.* **2014**, *55*, 4255–4259. [CrossRef]

40. Carbajo, D.; Ruiz-Sánchez, A.J.; Nájera, F.; Pérez-Inestrosa, E.; Alfonso, I. Spontaneous Macrocyclization through Multiple Dynamic Cyclic Aminal Formation. *Chem. Commun.* **2021**, *57*, 1190–1193. [CrossRef]

41. Mukhopadhyay, S.; Biswas, A.; Pandey, R.; Gupta, R.K.; Pandey, D.S. A Highly Selective and Femto-Molar Sensitive Fluorescence 'Turn-on' Chemodosimeter for Hg^{2+}. *Tetrahedron Lett.* **2014**, *55*, 1437–1440. [CrossRef]

42. Heng, S.; Reineck, P.; Vidanapathirana, A.K.; Pullen, B.J.; Drumm, D.W.; Ritter, L.J.; Schwarz, N.; Bonder, C.S.; Psaltis, P.J.; Thompson, J.G.; et al. Rationally Designed Probe for Reversible Sensing of Zinc and Application in Cells. *ACS Omega* **2017**, *2*, 6201–6210. [CrossRef]

43. Sun, F.; Zhang, G.; Zhang, D.; Xue, L.; Jiang, H. Aqueous Fluorescence Turn-on Sensor for Zn^{2+} with a Tetraphenylethylene Compound. *Org. Lett.* **2011**, *13*, 6378–6381. [CrossRef]

44. Shellaiah, M.; Wu, Y.-H.; Lin, H.-C. Simple Pyridyl-Salicylimine-Based Fluorescence "Turn-on" Sensors for Distinct Detections of Zn^{2+}, Al^{3+} and OH$^-$ Ions in Mixed Aqueous Media. *Analyst* **2013**, *138*, 2931–2942. [CrossRef] [PubMed]

45. Xu, J.; Xiong, J.; Qin, Y.; Li, Z.; Pan, C.; Huo, Y.; Zhang, H. A Novel Quinolinyl-Tetraphenylethene-Based Fluorescence "Turn-on" Sensor for Zn^{2+} with a Large Stokes Shift and Its Applications for Portable Test Strips and Biological Imaging. *Mater. Chem. Front.* **2020**, *4*, 3338–3348. [CrossRef]

46. Pandey, R.; Kumar, P.; Singh, A.K.; Shahid, M.; Li, P.; Singh, S.K.; Xu, Q.; Misra, A.; Pandey, D.S. Fluorescent Zinc(II) Complex Exhibiting "*On-Off-On*" Switching Toward Cu^{2+} and Ag$^+$ Ions. *Inorg. Chem.* **2011**, *50*, 3189–3197. [CrossRef] [PubMed]

47. Corrsin, L.; Fax, B.J.; Lord, R.C. The Vibrational Spectra of Pyridine and Pyridine-d5. *J. Chem. Phys.* **2004**, *21*, 1170–1176. [CrossRef]

48. Wong, P.T.T.; Brewer, D.G. Nature of the Coordination Bond in Metal Complexes of Substituted Pyridine Derivatives. IV. Skeletal Vibration Spectra and the Substituent Effect upon the Coordination Bond of the Pyridine Complex of Zinc(II) Ion. *Can. J. Chem.* **1969**, *47*, 4589–4597. [CrossRef]

49. Frisch, M.J.; Trucks, G.W.; Schlegel, H.B.; Scuseria, G.E.; Robb, M.A.; Cheeseman, J.R.; Scalmani, G.; Barone, V.; Petersson, G.A.; Nakatsuji, H.; et al. *Gaussian 16*; Revision B.01; Gaussian, Inc.: Wallingford, CT, USA, 2016.

50. Becke, A.D. Density-functional Thermochemistry. III. The Role of Exact Exchange. *J. Chem. Phys.* **1993**, *98*, 5648–5652. [CrossRef]

51. Lee, C.T.; Yang, W.T.; Parr, R.G. Development of the Colle-Salvetti Correlation-Energy Formula into a Functional of the Electron-Density. *Phys. Rev. B* **1988**, *37*, 785–789. [CrossRef]

52. Cossi, M.; Scalmani, G.; Rega, N.; Barone, V. New Developments in the Polarizable Continuum Model for Quantum Mechanical and Classical Calculations on Molecules in Solution. *J. Chem. Phys.* **2002**, *117*, 43–54. [CrossRef]

53. Miertuš, S.; Scrocco, E.; Tomasi, J. Electrostatic Interaction of a Solute with a Continuum. A Direct Utilizaion of AB Initio Molecular Potentials for the Prevision of Solvent Effects. *Chem. Phys.* **1981**, *55*, 117–129. [CrossRef]

54. McLean, A.D.; Chandler, G.S. Contracted Gaussian Basis Sets for Molecular Calculations. I. Second Row Atoms, Z = 11–18. *J. Chem. Phys.* **1980**, *72*, 5639–5648. [CrossRef]

55. Pettersen, E.F.; Goddard, T.D.; Huang, C.C.; Meng, E.C.; Couch, G.S.; Croll, T.I.; Morris, J.H.; Ferrin, T.E. UCSF ChimeraX: Structure Visualization for Researchers, Educators, and Developers. *Protein Sci.* **2021**, *30*, 70–82. [CrossRef] [PubMed]

56. Volpi, G.; Garino, C.; Nervi, C. Exploring Synthetic Pathways to Cationic Heteroleptic Cyclometalated Iridium Complexes Derived from Dipyridylketone. *Dalton Trans.* **2012**, *41*, 7098–7108. [CrossRef] [PubMed]

57. Volpi, G.; Garino, C.; Gobetto, R.; Nervi, C. Dipyridylmethane Ethers as Ligands for Luminescent Ir Complexes. *Molecules* **2021**, *26*, 7161. [CrossRef] [PubMed]

58. Hasan, M.M.; Kubra, K.T.; Hasan, M.N.; Awual, M.E.; Salman, M.S.; Sheikh, M.C.; Rehan, A.I.; Rasee, A.I.; Waliullah, R.M.; Islam, M.S.; et al. Sustainable Ligand-Modified Based Composite Material for the Selective and Effective Cadmium(II) Capturing from Wastewater. *J. Mol. Liq.* **2023**, *371*, 121125. [CrossRef]

59. Montaño-Medina, C.U.; Lopéz-Martínez, L.M.; Ochoa-Terán, A.; López-Maldonado, E.A.; Salazar-Gastelum, M.I.; Trujillo-Navarrete, B.; Pérez-Sicairos, S.; Cornejo-Bravo, J.M. New Pyridyl and Aniline-Functionalized Carbamoylcarboxylic Acids for Removal of Metal Ions from Water by Coagulation-Flocculation Process. *Chem. Eng. J.* **2023**, *451*, 138396. [CrossRef]

60. Hozien, Z.A.; EL-Mahdy, A.F.M.; Ali, L.S.A.; Markeb, A.A.; El-Sherief, H.A.H. One-Pot Synthesis of Some New *s*-Triazole Derivatives and Their Potential Application for Water Decontamination. *ACS Omega* **2021**, *6*, 25574–25584. [CrossRef]

61. Volpi, G.; Ginepro, M.; Tafur-Marinos, J.; Zelano, V. Pollution Abatement of Heavy Metals in Different Conditions by Water Kefir Grains as a Protective Tool against Toxicity. *J. Chem.* **2019**, *2019*, 8763902. [CrossRef]

62. Costamagna, G.; Volpi, G.; Ghibaudi, E.; Ginepro, M. Quantitative Insights on the Interaction between Metal Ions and Water Kefir Grains: Kinetics Studies and EPR Investigations. *Nat. Prod. Res.* **2022**, *36*, 3440–3444. [CrossRef]

63. Bianco Prevot, A.; Ginepro, M.; Peracaciolo, E.; Zelano, V.; De Luca, D.A. Chemical vs Bio-Mediated Reduction of Hexavalent Chromium. An In-Vitro Study for Soil and Deep Waters Remediation. *Geoderma* **2018**, *312*, 17–23. [CrossRef]

64. Gul, Z.; Salman, M.; Khan, S.; Shehzad, A.; Ullah, H.; Irshad, M.; Zeeshan, M.; Batool, S.; Ahmed, M.; Altaf, A.A. Single Organic Ligands Act as a Bifunctional Sensor for Subsequent Detection of Metal and Cyanide Ions, a Statistical Approach toward Coordination and Sensitivity. *Crit. Rev. Anal. Chem.* **2023**, 1–17. [CrossRef]